



## Competitive adsorption of methane and ethane on organic-rich shale at pressure up to 30 MPa: Experimental results and geological implications

Jing Li <sup>a,b</sup>, Pengpeng Li <sup>c</sup>, Shixin Zhou <sup>a,b,\*</sup>, Zexiang Sun <sup>a,b</sup>, Bingkun Meng <sup>a,b,d</sup>, Yaoyu Li <sup>a,b,d</sup>

<sup>a</sup> Northwest Institute of Eco-Environment and Resources, Chinese Academy of Sciences, Lanzhou, China

<sup>b</sup> Key Laboratory of Petroleum Resources, Gansu Province, Lanzhou, China

<sup>c</sup> Institute of Energy, Peking University, Beijing, China

<sup>d</sup> University of Chinese Academy of Sciences, Beijing, China



### ARTICLE INFO

#### Keywords:

Shale gas  
Binary adsorption  
Supercritical conditions  
Gas-in-place  
Controlling factors

### ABSTRACT

Methane and ethane are the two most abundant hydrocarbon species in shale gas, while the adsorption behavior of their binary mixture in shale is still ambiguous. In this study, the adsorptions of methane, ethane, and their binary mixture on twelve dried mature lacustrine organic-rich shale samples were measured at 60 °C and variable pressures ranging from 0.001 to 30 MPa. The Langmuir and supercritical Dubinin–Radushkevich (SDR) models combined with the ideal adsorbed solution theory (IAST) and Extended Langmuir (EL) model were used to describe the raw adsorption isotherms. By contrast, the Langmuir model with consistent adsorbed phase volume can better describe the ethane excess adsorption. The IAST and EL models matched binary gas excess adsorption equally well. The adsorption capacity of pure ethane was about 1.6 times as large as pure methane, while the Langmuir pressure for ethane was lower. For the adsorption of pure and binary gas, organic matter was the primary contributor, followed by clay minerals. The adsorption selectivity of ethane over methane ranged from 3.49 to 8.85, which strongly depended on total organic carbon (TOC), and weakly negatively correlated with clay mineral content. The estimated gas-in-place (GIP) of binary gas ranged from 4.57 cm<sup>3</sup>/g to 8.08 cm<sup>3</sup>/g, which was about 30% larger than that of pure methane. A two-stage trend, first falling and then rising, was observed in relationship between binary gas GIP and TOC. This phenomenon could be attributed to the opposite effects of residual bitumen on shale porosity and gas adsorption. This study provides better insight in the storage mechanisms of shale gas and a basis for the reliable estimation of shale gas potential.

### 1. Introduction

Due to developments in horizontal drilling and hydraulic fracturing techniques, shale gas output has steadily expanded over the last several decades [1,2]. In 2020, U.S. shale gas production reached 26,139 billion cubic feet (Bcf) and accounted for 78.06% of the total U.S. natural gas production [3]. In the same year, shale gas production in China reached  $200 \times 10^8$  m<sup>3</sup>, making China the second-largest shale gas producer in the world [4]. Gas trapped in shale formations exists in three phases: free gas in pores and fractures, adsorbed gas on various surfaces, and absorbed gas dissolved in organic matter and any liquids. Notably, adsorbed gas could account for 85% of total shale gas [1]. Thus, gas adsorption behavior in shale is essential for the evaluation of shale gas potential and exploitation in shale gas reservoirs.

Much attention has been paid to methane adsorption on shale and its

components, such as kerogen and clay minerals [5–21]. Based on experiment or molecular simulation, researchers quantified adsorption behavior of methane on kerogen [5–8], clays [9–11] and shale from various regions [12–14], investigated the factors influencing methane adsorption [15–18], and estimated the gas storage capacity of shale under reservoir conditions (or so-called gas-in-place, abbreviated as GIP) [19–21]. However, gas trapped in shale formations is a complex mixture in which methane proportions can vary from 36.7% to 99.3% [22,23]. The proportions of ethane, which is the second primary hydrocarbon species, could be up to 16.1% in U.S. shale gas [22]. In the Yangchang shale gas play located in the Southern Ordos Basin, China, the average content of methane is 80.17% in shale gas, while ethane content could reach 17.62% [24]. The presence of ethane may modify methane sorption behavior in shale due to its greater affinity [25]. Understanding competitive sorption properties between ethane and

\* Corresponding author at: Northwest Institute of Eco-Environment and Resources, Chinese Academy of Sciences, Lanzhou, China.

E-mail address: zhoushixin@nieer.ac.cn (S. Zhou).

methane in shale is essential for an accurate assessment of shale gas potential and the development of extraction methods.

At present, only limited reports are available about the adsorption of methane/ethane binary mixture in shale medium. Collell et al. [26] investigated the microporous adsorption procedures of pure methane, ethane and their binary mixture on mature kerogen via molecular simulation and examined the predictions of the ideal adsorbed solution theory (IAST) and an improved Extended Langmuir (EL) model. Wang et al. [27] illustrated methane/ethane competitive sorption on one Marcellus shale sample via the experimental methods and the multi-component potential theory of adsorption (MPTA) model. In the follow-up study [28], they further investigated the sorption kinetics of methane/ethane mixtures. Wang et al. [29] investigated the adsorption behavior of pure and binary mixtures of methane and ethane in montmorillonite slits with apertures ranging from 1.1 nm to 3.0 nm. Some factors were discussed to evaluate their effects on adsorption isotherms and selectivity, such as pore size, pressure, temperature, fluid composition, and water content. Huang et al. [30] analyzed the sorption of methane, ethane and their mixture on three black shale samples via a volumetric method, in which three-parameter Langmuir model and EL model were adopted to fit the data, and discuss the effect of gas composition and pressure on sorption. Currently, GIP estimation based on methane/ethane binary mixture adsorption is still a gap. Moreover, shale composition and nanopore characteristics significantly affect gas adsorption behavior [18]. The relationships between shale composition, nanopore characteristics and methane/ethane competitive sorption are still unclear.

Lacustrine shales from the Upper Triassic Yanchang Formation in the Ordos Basin are some of the most important petroleum resources in China. Preliminary investigations have indicated good shale gas potential [31]. The shale gases from the Yanchang Formation are dominated by methane, with a dryness (defined as the volume ratio of methane to all hydrocarbon gases) range of 0.64–0.8 [24]. Therefore, understanding

the methane/ethane competitive sorption on shale is critical for accurate resource evaluation of the Yanchang shale gas play.

In the present study, the adsorption of pure methane, ethane and their binary mixture on 12 shale samples from the Yanchang Formation were measured by a gravimetric method at 60 °C and variable pressures ranging from 0.001 to 30 MPa. As mentioned above, the average methane content of shale gas from the Yanchang Formation is 80.17%, and ethane content could be up to 17.62% [24]. Then a binary mixture of 80% methane and 20% ethane was adopted in the adsorption measurements. The goals were (1) to quantify the methane/ethane binary adsorption on the Yanchang shale, (2) to understand the effects of shale composition and nanopore characteristics on binary gas adsorption, and (3) to estimate the binary gas GIP of the shale and investigate its controls.

## 2. Samples and methods

### 2.1. Samples

The YK-1 well is a full core extraction well drilling from the Chang 4 + 5 Subsection to the Chang 10 Subsection of the Upper Triassic Yangchang Formation. Systematic sampling of the Yanchang Shale can be conducted in cores of the YK-1 well. In this study, twelve representative shale core samples collected from the YK-1 well were utilized. The detailed sampling location and formation was shown in Fig. 1.

The studied shale samples are typical organic-rich lacustrine shale. The organic geochemistry data and mineralogical compositions for the studied shale samples were shown in Appendix A. Supplementary Material. In brief, the studied samples have high TOC ranging from 0.84% to 23.9% and are within the oil window ( $T_{max}$  ranges from 433 °C to 442 °C). The organic type of the studied samples is mainly type I. The mineral compositions of the studied samples are mainly clay minerals (including illite, chlorite, kaolinite, and smectite), quartz, and pyrite,

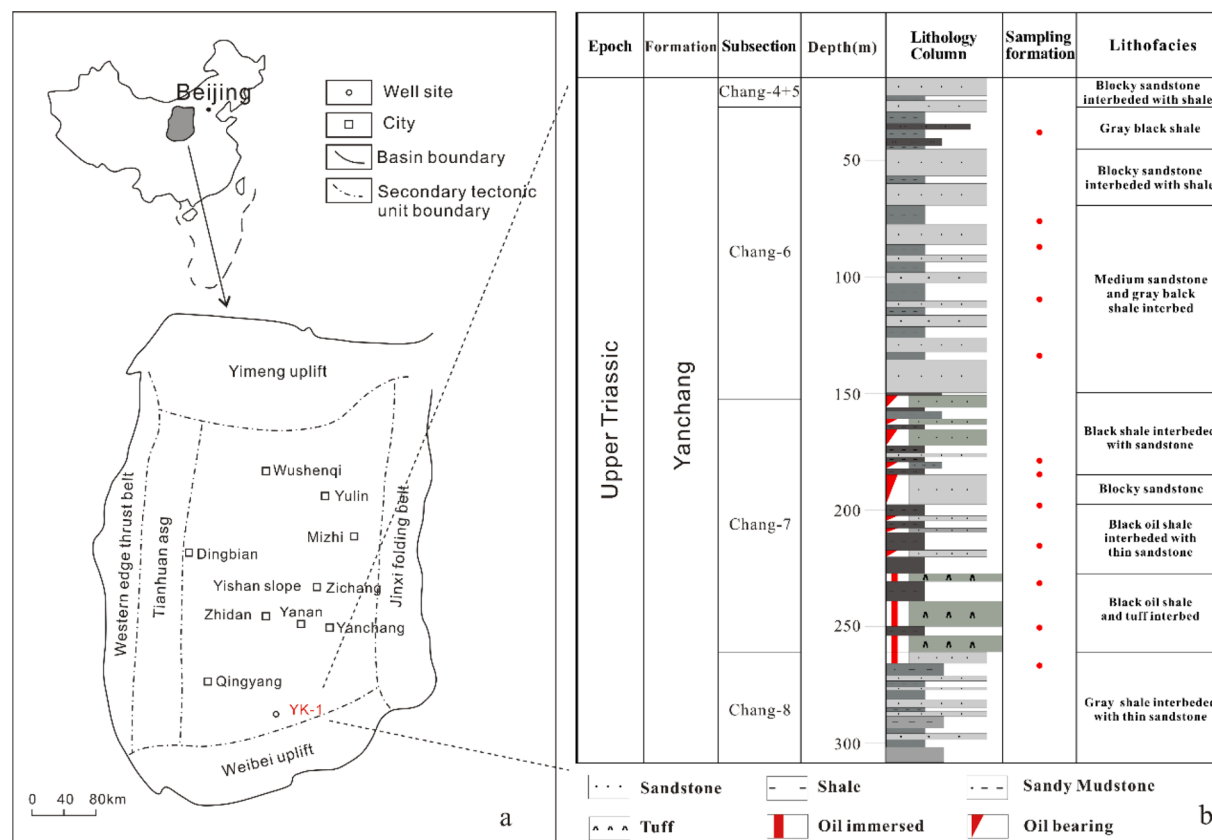


Fig. 1. Sampling location (a) and stratigraphic section (b).

whose contents are 24.77–59.31%, 19.01–44.48%, and 0–39.76%, respectively. The detailed description could be seen in literature [32].

Nanopore characteristics of the shale samples were obtained via low pressure N<sub>2</sub> adsorption measurement combined with the Brunauer–Emmett–Teller (BET), Barrett–Joyner–Halenda (BJH), Dubinin–Astakhov (DA) and density functional theory (DFT) models [32]. The detailed information for these models can be checked in the references [33–36]. The nanopore characteristics were shown in Appendix A, Supplementary Material (Table A2). In brief, nanopores in the studied shale samples are dominated by mesopores according to the pore classification proposed by IUPAC [37]. Average pore diameter (APD) ranges from 6.9 nm to 21.8 nm. Total specific surface area (SSA) calculated via the BET model is 0.93–15.43 m<sup>2</sup>/g with a mean of 4.34 m<sup>2</sup>/g. Pore volume (PV) for pores with a diameter ranging from 1.7 nm to 300 nm calculated via the BJH model is 0.0042–0.0281 cm<sup>3</sup>/g with a mean of 0.0127 cm<sup>3</sup>/g. PV for micropores calculated via the DA model is 0.0003–0.0068 cm<sup>3</sup>/g with a mean of 0.0020 cm<sup>3</sup>/g. Argon ion polishing field emission scanning electron microscope (FE-SEM) images for the studied samples were presented in Fig. A1. In brief, organic matter pores, intraparticle pores related to clay mineral and interparticle pores at edge of rigid grain were observed. Detailed description for the FE-SEM images could be checked in reference [38].

## 2.2. Gas adsorption measurements

The shale samples were crushed to 60 mesh (grain size smaller than 0.15 mm). Then, the adsorption experiments of methane, ethane, and their binary mixture composed of 80% methane and 20% ethane were carried out at temperature of 60 °C and pressures ranging from 0.001 to 30 MPa via a gravimetric high-pressure sorption analyzer (Rubotherm, ISOSORP-HP III Static) with a magnetic suspension balance. Three steps, so-called pretreatment, buoyancy measurement and adsorption measurement, were sequentially performed during the measurement procedure. In the pretreatment step, about 5 g of sample were placed in a vacuum measuring cell and degassed for 20 h at 110 °C to remove adsorbed moisture and volatile matter. During the buoyancy measurement step, the accurate mass and volume of the sample were measured using helium (99.999%) within a pressure range of 0.001 ~ 7 MPa based on the Archimedes principle. During the adsorption measurement step, the adsorption amounts of pure or binary gas mixture were measured at 60 °C and 0.001 ~ 30 MPa based on the gravimetric method [39–42]. The adsorption data were recorded at 15 designated pressure points. At each pressure point, an adsorption time of 2 h was given, after which the adsorption equilibrium was assumed to be achieved.

Free gas density is essential for quantifying gas adsorption. In this study, free densities of methane, ethane and their binary mixture were measured by the sinker of the sorption analyzer during the adsorption measurements. Corresponding details can be found in literature [40].

The total adsorbed amount of binary gas mixture could be directly measured by the adsorption experiments. The partial adsorbed amount of methane or ethane was obtained via binary gas mixture adsorption models, such as the extended Langmuir (EL) model and the Ideal Adsorbed Solution Theory (IAST) in this study.

## 2.3. Models for pure gas adsorption

In the gas adsorption tests, the measured quantities are excess adsorption capacities ( $n_{ex}$ ) [43]. The relation between  $n_{ex}$  and the absolute adsorption capacities ( $n_{abs}$ ) is given by Eqs. (1) and (2).

$$n_{ex} = n_{abs} - V_{ad} \cdot \rho_g \quad (1)$$

$$n_{ex} = n_{abs} \left( 1 - \frac{\rho_g}{\rho_{ad}} \right) \quad (2)$$

Here,  $V_{ad}$  is the volume of adsorbed phase,  $\rho_{ad}$  is the density of adsorbed

phase, and  $\rho_g$  is the density of free adsorbate, which could be experimentally measured in this study.

The Langmuir model and supercritical Dubinin–Radushkevich (SDR) equation are widely used to describe absolute adsorption isotherm of pure gas [5,12,44–47], which are shown in Eq. (3) and Eq. (4), respectively.

$$n_{abs} = n_0 \cdot \frac{P}{P_L + P} \quad (3)$$

$$n_{abs} = n_0 \cdot \exp \left\{ - D \cdot \left[ \ln \left( \frac{\rho_{ad}}{\rho_g} \right) \right]^2 \right\} \quad (4)$$

Here,  $n_0$  is the maximum absolute adsorption capacity at a given temperature,  $P$  is the equilibrium pressure,  $P_L$  is the Langmuir pressure at which the amount of adsorbed gas equals half of the maximum adsorption capacity.  $D$  is a constant related to the affinity of the sorbent for the gas.

Substituting Eq. (3) into Eqs. (1) and (2) gives the Langmuir-based excess adsorption models (Eqs. (5) and (6)).

$$n_{ex} = n_0 \cdot \frac{P}{P_L + P} - V_{ad} \cdot \rho_g \quad (5)$$

$$n_{ex} = n_0 \cdot \frac{P}{P_L + P} \left( 1 - \frac{\rho_g}{\rho_{ad}} \right) \quad (6)$$

The assumption that the volume ( $V_{ad}$ ) or the density ( $\rho_{ad}$ ) of adsorbed phase is constant during the measurement is required when using Eq. (5) or (6) to fix excess adsorption isotherms [21,48]. Eqs. (5) and (6) were respectively referred to as the Langmuir-V<sub>ad</sub> model and the Langmuir-ρ<sub>ad</sub> model in this study.

Substituting Eq. (4) into Eqs. (1) and (2) gives the SDR-based excess adsorption model (Eqs. (7) and (8)).

$$n_{ex} = n_0 \cdot \exp \left\{ - D \cdot \left[ \ln \left( \frac{\rho_{ad}}{\rho_g} \right) \right]^2 \right\} - V_{ad} \cdot \rho_g \quad (7)$$

$$n_{ex} = n_0 \cdot \exp \left\{ - D \cdot \left[ \ln \left( \frac{\rho_{ad}}{\rho_g} \right) \right]^2 \right\} \cdot \left( 1 - \frac{\rho_g}{\rho_{ad}} \right) \quad (8)$$

Eq. (8) could be used to fix excess adsorption isotherms and obtain absolute adsorption isotherms when the density of adsorbed phase ( $\rho_{ad}$ ) is assumed as a constant during the measurement. However, once the volume of adsorbed phase ( $V_{ad}$ ) is regarded as a constant, the density of adsorbed phase ( $\rho_{ad}$ ) is variable, leading to the invalidation of Eq. (7) in the fixing of excess adsorption isotherms. To avoid that, a constant was introduced, named maximum density of adsorbed phase ( $\rho_{ad0}$ , Eq. (9)). Then Eq. (7) could transform into Eq. (10), which is suitable for fixing excess adsorption isotherms.

$$\rho_{ad0} = \frac{n_0}{V_{ad}} \quad (9)$$

$$n_{ex} = V_{ad} \cdot \rho_{ad0} \cdot \exp \left\{ - D \cdot \left[ \ln \left( \frac{\rho_{ad0}}{\rho_g} \right) \right]^2 \right\} - V_{ad} \cdot \rho_g \quad (10)$$

Eqs. (10) and (8) were respectively referred to as the SDR-V<sub>ad</sub> model and the SDR-ρ<sub>ad</sub> model in this study.

## 2.4. Models for binary gas mixture adsorption

In this study, the EL model and the IAST were used to predict the adsorption of binary gas mixture. The adsorbed phase of binary gas was assumed to be ideal mixing, and the mixture density was calculated via pure gas adsorption data [49]. The excess adsorption of binary gas was obtained via Eq. (2), and the comparison was performed between the theoretical result and experimental quantity to check the validation of

those models.

The EL model is the simplest model for the prediction of multicomponent adsorption isotherms [50,51]. Eq. (11) is one expression of the EL model.

$$n_i = \frac{n_{0i} \cdot b_i \cdot P_i}{1 + \sum_j^{N_c} b_j \cdot P_j} \quad (11)$$

Here,  $n_i$  is amount of component  $i$  in the adsorbed phase mixture;  $n_{0i}$  is maximum absolute adsorption capacity of component  $i$  in pure gas adsorption;  $b_i$  is the Langmuir constant of component  $i$  in pure gas adsorption and equals the reciprocal of  $P_L$ ;  $N_c$  is the number of components;  $P_i$  is partial pressure of component  $i$  in the free gas phase and it can be determined via Eq. (12).

$$P_i = P \cdot y_i \quad (12)$$

Here,  $P$  is pressure of the free gas phase;  $y_i$  is mole fraction of component  $i$  in the free gas phase.

The IAST is one of the most reliable and common methods for predicting multicomponent adsorption [52]. This theory is based on the assumption that the adsorbed phase is an ideal solution in which interactions between molecules are equivalent in strength [53]. The method for determining multicomponent adsorption using the IAST has been discussed in detail in a variety of literatures [51,52,54]. The most common form of the IAST model is shown in Eqs. (13)–(16).

$$P \cdot y_i = P_i^o(\pi) \cdot x_i \quad (13)$$

$$\pi_i(P_i^o) = \int_0^{P_i^o} \frac{n_i(P)}{P} dP \quad (14)$$

$$\frac{1}{n_t} = \sum_{i=1}^{N_c} \frac{x_i}{n_i^o} \quad (15)$$

$$n_i = n_t \cdot x_i \quad (16)$$

Here,  $P_i^o(\pi)$  is gas pressure of the pure component  $i$  adsorbed at the same temperature and spreading pressure as the mixture;  $x_i$  is mole fraction of component  $i$  in the adsorbed phase;  $\pi_i(P_i^o)$  is the spreading pressure and can be calculated using pure gas adsorption isotherm of component  $i$  according to Eq. (14);  $n_i(P)$  is adsorbed amount of pure component  $i$  at pressure  $P$ ;  $n_t$  is the total adsorbed amount in mixed gas adsorption system;  $n_i^o$  is adsorbed amount of pure component  $i$  at the constant spreading pressure;  $n_i$  is adsorbed amount of component  $i$  in the mixed gas adsorption system.

The adsorbed phase of binary gas was assumed to be an ideal mixing, and its density,  $\rho_{ad-bin}$ , could be calculated by the adsorbed phase densities of the pure gas [49] according to Eq. (17).

$$\frac{1}{\rho_{ad-bin}} = \frac{x_{meth}}{\rho_{ad-meth}} + \frac{x_{eth}}{\rho_{ad-eth}} \quad (17)$$

Here,  $x_{meth}$  and  $x_{eth}$  are mole fractions of methane and ethane in the adsorbed phase of binary gas respectively, and they could be calculated via the EL model or the IAST;  $\rho_{ad-meth}$  and  $\rho_{ad-eth}$  are adsorbed phase densities of methane and ethane in pure gas adsorption, which were obtained via the Langmuir-based or the SDR-based excess adsorption models and excess adsorption isotherms.

The adsorption selectivity of ethane against methane ( $S_{eth/meth}$ ) was calculated via Eq. (18) to quantitatively characterize their competitive adsorption in the binary gas mixture [55].

$$S_{eth/meth} = \frac{x_{eth}/x_{meth}}{y_{eth}/y_{meth}} \quad (18)$$

Here,  $y_{meth}$  and  $y_{eth}$  are mole fractions of methane and ethane in the free phase of binary gas, and they are 0.8 and 0.2 in this study, respectively.

## 2.5. Calculations of fitting errors

The fitting errors ( $\Delta n$ ) of the models were calculated by Eq. (19).

$$\Delta n = \frac{1}{N} \sum_i^N |n_i^{exp}(P_i, T_i) - n_i^{fit}(P_i, T_i)| \quad (19)$$

Here,  $n_i^{exp}(P_i, T_i)$  and  $n_i^{fit}(P_i, T_i)$  represent the measured and fitted excess adsorption amount of methane, ethane or binary gas at the  $i$ th paired temperature and pressure, respectively.

The average relative deviations (ARD) of the models' predictions were calculated by Eq. (20).

$$ARD = \frac{1}{N} \sum_i^N \left| \frac{n_i^{exp}(P_i, T_i) - n_i^{fit}(P_i, T_i)}{n_i^{exp}(P_i, T_i)} \right| \cdot 100\% \quad (20)$$

## 3. Results

### 3.1. Pure gas adsorption

#### 3.1.1. Characteristics of pure gas excess adsorption isotherms

The measured excess adsorption isotherms for pure methane and ethane on the shale samples were shown in Fig. A2. With the increasing pressures, excess adsorptions of methane and ethane increased first, reaching maximum values, then decreased. This excess adsorption isotherm shapes are very common in high pressure gas adsorption measurements [6,12,29,42,47,56]. They occur because free gas densities and adsorbed gas densities converge with increasing pressures [21]. According to Eqs. (1) and (2), excess adsorption could approach zero when the free density is high enough. A steep decline followed by an inflection was observed in the decline part of ethane excess adsorption isotherms. This occurrence is related to the steep increase and inflection in ethane density variation in the corresponding pressure range (Fig. A3a, c). The free methane density almost linearly increased in the whole pressure range in this study (Fig. A3a), leading to a linear decline of methane excess adsorption under the high-pressure condition (Fig. A3b).

Methane excess adsorption reached its maximum at pressure around 10–15 MPa, while the maximum excess adsorption of ethane appeared around 5 MPa (Fig. A2). This difference is attributed to both the more rapid rise in ethane absolute adsorption compared to methane and the relatively slow rise in free ethane density in low-pressure range (Fig. A3b, c). The maximum excess adsorption for ethane is higher than for methane in the pure gas adsorption isotherms for a given sample (Fig. A2). Given that free densities for both methane and ethane are relatively low in the corresponding pressure range (Fig. A3b, c), this occurrence is mainly related to the higher maximum absolute adsorption capacity for ethane (Table 1), which is an indication for stronger affinity of shale towards ethane [27]. At high pressure, such as pressure of 30 MPa, free density for ethane is significantly higher than for methane (Fig. A3a) and the value of adsorbed phase volume times free ethane density approached ethane absolute adsorption (Fig. A3c), resulting in the lower excess adsorption for ethane than for methane (Fig. A2).

#### 3.1.2. Fitting results of pure gas excess adsorption isotherms for various models

For methane adsorption isotherms, although the fitted maximum absolute adsorption capacities ( $n_0$ ) showed small difference for different models, the fitting effects were equally good (Fig. 2), which is consistent with previous findings [20,21]. All the fitted curves of methane excess adsorption were closed to the experimental isotherms (Fig. 2). The average fitting errors ( $\Delta n$ ) and average relative deviations (ARD) were 0.0008 mmol/g and 1.63 % for the Langmuir- $\rho_{ad}$  model, 0.0009 mmol/g and 2.22 % for the SDR- $\rho_{ad}$  model, 0.0009 mmol/g and 1.69 % for the Langmuir- $V_{ad}$  model, 0.0010 mmol/g and 2.34 % for the SDR- $V_{ad}$  model, respectively (Table 1). The fitting errors of methane adsorption

**Table 1**

Fitted parameters of the Langmuir-based and SDR-based models for pure methane excess adsorption.

		YK4	YK16	YK18	YK22	YK29	YK42	YK49	YK55	YK78	YK93	YK101	YK107
Langmuir- $\rho_{ad}$ model	$n_0$ (mmol/g)	0.196	0.213	0.192	0.250	0.142	0.200	0.206	0.160	0.244	0.298	0.287	0.217
	$p_L$ (MPa)	8.62	9.23	9.55	7.33	9.58	8.94	8.90	9.46	8.58	5.68	7.56	7.51
	$\rho_{ad}$ (mmol/cm <sup>3</sup> )	20.29	20.84	20.93	21.32	20.61	21.79	21.03	21.20	22.13	21.55	21.91	22.15
	$\Delta n$ (mmol/g)	0.0009	0.0004	0.0005	0.0007	0.0003	0.0007	0.0009	0.0005	0.0008	0.0017	0.0011	0.0011
SDR- $\rho_{ad}$ model	$n_0$ (mmol/g)	0.145	0.155	0.139	0.196	0.101	0.148	0.149	0.116	0.185	0.253	0.226	0.171
	$D$	0.117	0.119	0.120	0.110	0.117	0.113	0.110	0.117	0.111	0.102	0.109	0.106
	$\rho_{ad}$ (mmol/cm <sup>3</sup> )	22.38	23.23	23.41	23.00	23.46	24.55	24.20	24.00	24.70	22.00	23.78	24.23
	$\Delta n$ (mmol/g)	0.0011	0.0006	0.0008	0.0008	0.0006	0.0010	0.0010	0.0006	0.0010	0.0014	0.0012	0.0012
Langmuir- $V_{ad}$ model	$n_0$ (mmol/g)	0.249	0.276	0.237	0.299	0.147	0.214	0.223	0.208	0.268	0.339	0.345	0.260
	$p_L$ (MPa)	9.50	10.29	10.00	7.83	8.04	8.00	8.02	10.60	8.00	5.94	8.11	8.00
	$V_{ad}$ (cm <sup>3</sup> /g)	0.011	0.012	0.010	0.013	0.006	0.008	0.009	0.009	0.010	0.014	0.014	0.011
	$\Delta n$ (mmol/g)	0.0009	0.0004	0.0005	0.0009	0.0007	0.0011	0.0011	0.0004	0.0011	0.0017	0.0011	0.0012
SDR- $V_{ad}$ model	$n_0$ (mmol/g)	0.159	0.170	0.154	0.214	0.111	0.162	0.163	0.128	0.201	0.272	0.246	0.186
	$D$	0.119	0.120	0.123	0.112	0.118	0.114	0.111	0.120	0.112	0.102	0.110	0.108
	$V_{ad}$ (cm <sup>3</sup> /g)	0.007	0.008	0.007	0.010	0.005	0.007	0.007	0.006	0.008	0.013	0.011	0.008
	$\rho_{ado}$ (mmol/cm <sup>3</sup> )	21.51	22.35	22.00	22.00	22.56	23.62	23.29	22.70	23.77	21.64	22.91	23.34
$\Delta n$ (mmol/g)	0.0011	0.0006	0.0008	0.0008	0.0006	0.0010	0.0010	0.0006	0.0011	0.0014	0.0012	0.0012	
	ARD (%)	2.79	1.76	2.74	1.73	2.44	2.98	2.53	1.99	2.55	1.80	2.05	2.79

$n_0$ : maximum absolute adsorption capacity;  $P_L$ : Langmuir pressure;  $\rho_{ad}$ : density of adsorbed gas phase;  $\Delta n$ : fitting error; ARD: average relative deviations;  $V_{ad}$ : volume of adsorbed gas phase;  $D$ : constant in SDR equations;  $\rho_{ado}$ : maximum density of adsorbed phase.

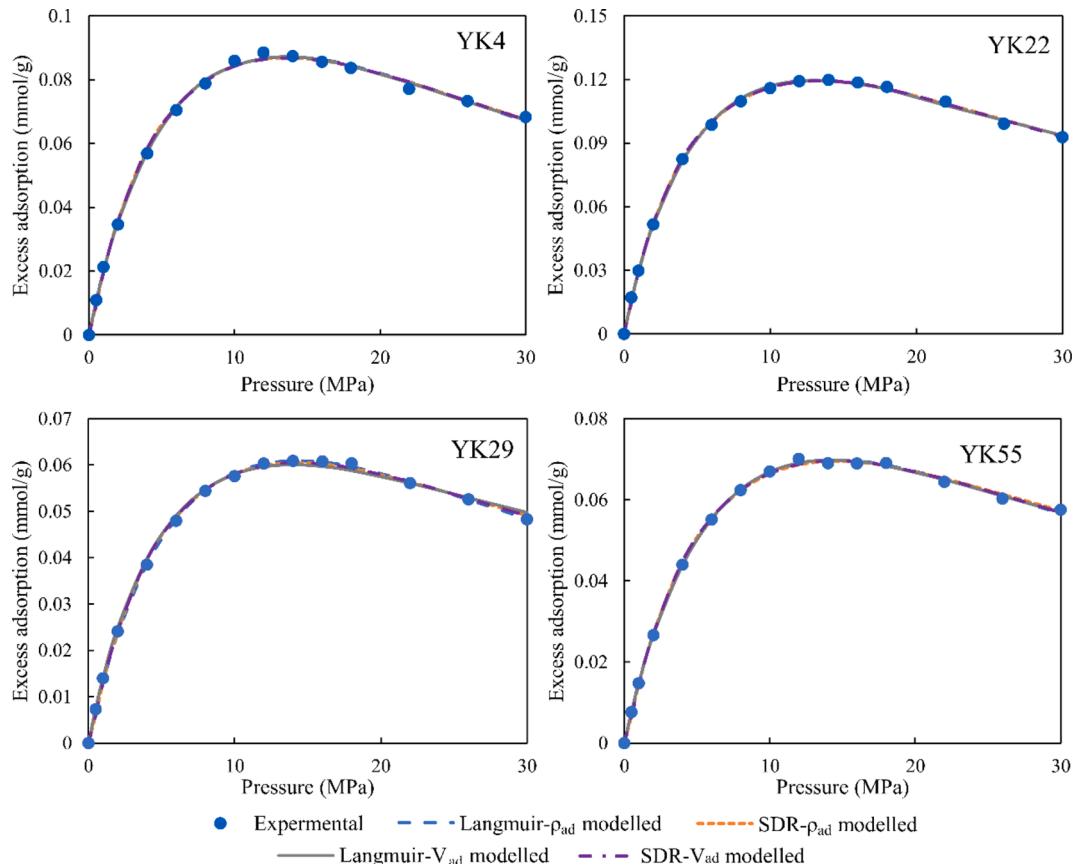


Fig. 2. Fitting results of methane excess adsorption isotherms at 60 °C for various models.

isotherms obtained in this study were smaller or close to the values reported in previous literatures [12,16,20].

For ethane adsorption isotherms, the Langmuir- $V_{ad}$  model suggested significantly better fitting result than other models (Fig. 3). The Langmuir- $V_{ad}$  model had an average  $\Delta n$  and ARD of 0.0054 mmol/g and 8.01%, which were significantly lower than the Langmuir- $\rho_{ad}$  model, SDR- $\rho_{ad}$  model and SDR- $V_{ad}$  model (0.0058 mmol/g and 12.30%, 0.0057 mmol/g and 12.42%, 0.0062 mmol/g and 13.42%, respectively, Table 2). Weniger et al. [56] and Clarkson and Haghshenas [47] also noted that excess adsorption models with a constant  $\rho_{ad}$  could not satisfactorily match some supercritical CO<sub>2</sub> isotherms, but the cause was not discussed. According to the assumption of constant  $\rho_{ad}$ , excess adsorption should show a linear decline with the increasing free density under the high-pressure condition. However, a upwarp is observed in ethane isotherm as marked with red circle in Fig. 4a. Similar upwarp has also been observed in supercritical CO<sub>2</sub> isotherm [47] and methane isotherm with pressure up to 60 MPa [21]. This “upwarp” implies that  $\rho_{ad}$  increase under the high-pressure condition [21]. This phenomenon could be the main reason for the poor fitting effect of models with a constant  $\rho_{ad}$ . To further prove it, ethane isotherm without the “upwarp” part was fitted by the corresponding models, and the fittings were remarkably improved (Fig. 4b).

The constant adsorption phase volume or density is an assumption made for the convenience of excess adsorption curve fitting. In practice, both of them may become larger as the adsorption increases. Under high adsorption conditions, the variation in adsorbed phase volume is limited because the pore volume is constant (ignoring sorption-induced swelling of shale matrix), then the variation in adsorbed phase density may increase. The assumption of constant adsorption phase volume may therefore be more consistent with the gas excess adsorption behavior at high adsorption condition, leading to a better fitting of model with a constant  $V_{ad}$ . The SDR model is applied to supercritical conditions by

converting P<sub>0</sub>/P in the DR model to  $\rho_{ad}/\rho_g$  [46]. In its underlying assumptions  $\rho_{ad}$  is defined as constant to correspond to P<sub>0</sub> in the DR model. Although in application of the present study a concept of  $\rho_{ad}$  was introduced based on assumption of constant  $V_{ad}$ , the assumptions underlying the SDR model dictate that it may not be applicable to excess adsorption behavior under high adsorption condition, resulting in its poor fit for the ethane isotherms.

The adsorption of ethane is significantly higher than that of methane at the same pressure. To achieve the state where adsorbed phase volume increase is limited, higher pressures are required for methane relative to ethane. In the present study, the “upwarp” appeared in ethane isotherms, but not in methane isotherms. As a result, all models match methane isotherms equally well, while for ethane isotherms only the Langmuir- $V_{ad}$  model fits good.

In this study, fitted parameters of the Langmuir- $V_{ad}$  model were used to characterize pure gas adsorption due to its good fitting effect.  $n_0$  of ethane ranged from 0.272 to 0.617 mmol/g with an average of 0.410 mmol/g, which was about 1.6 times larger than that of methane (0.147–0.345 mmol/g with an average of 0.255 mmol/g). While  $P_L$  of ethane was significantly lower than that for methane, the former was 2.73–4.74 MPa and the latter was 5.94–10.60 MPa. The above occurrences were consistent with the findings that Langmuir adsorption capacities for hydrocarbon gases increased with carbon number while Langmuir pressures showed a decreasing trend in shale [57].

### 3.2. Binary gas adsorption

#### 3.2.1. Fitting accuracies for the EL and IAST models

The shape of binary gas adsorption isotherms was similar to that of methane adsorption isotherms (Fig. A2). When binary gas excess adsorption amount reached its maximum value, the pressure was around 12 MPa and lied between the corresponding values of pure methane and

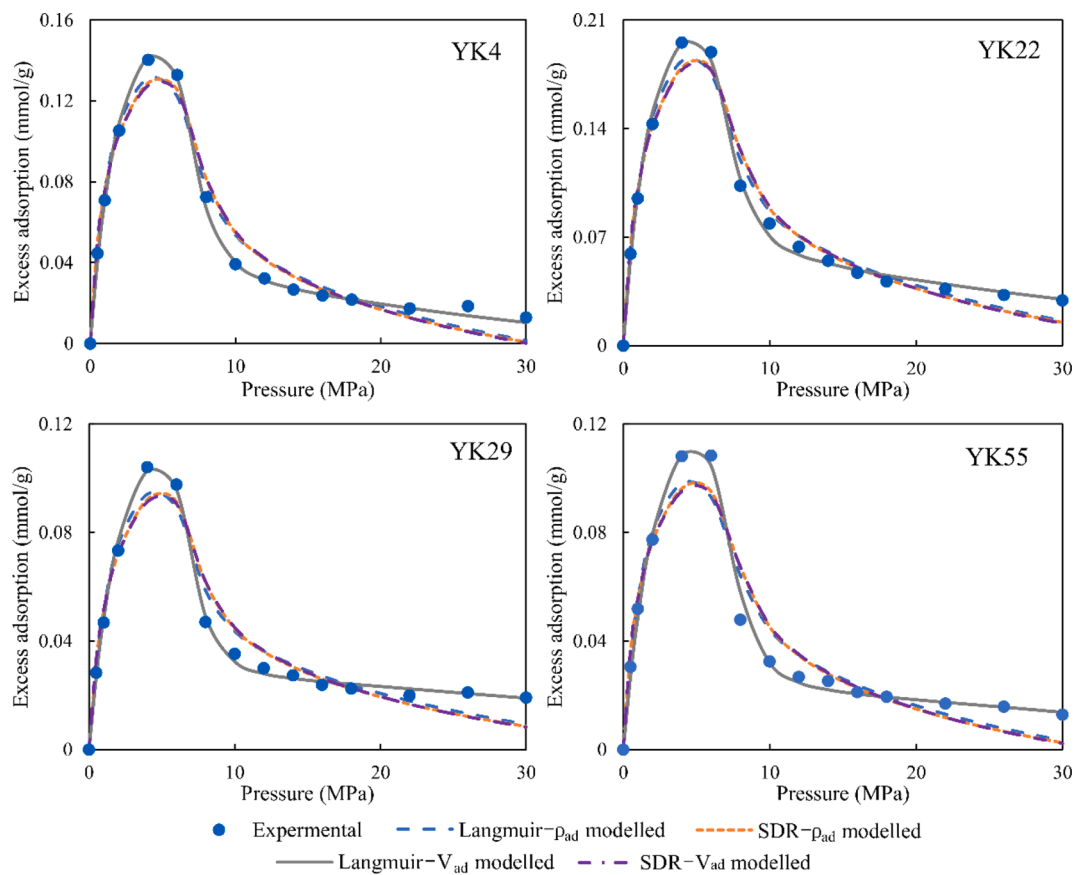


**Fig. 3.** Fitting results of ethane excess adsorption isotherms at 60 °C for various models.

**Table 2**

Fitted parameters of the Langmuir-based and SDR-based models for pure ethane excess adsorption.

		YK4	YK16	YK18	YK22	YK29	YK42	YK49	YK55	YK78	YK93	YK101	YK107
Langmuir- $\rho_{ad}$ model	$n_0$ (mmol/g)	0.230	0.309	0.285	0.333	0.172	0.308	0.299	0.173	0.357	0.550	0.499	0.461
	$p_L$ (MPa)	1.97	2.85	2.94	2.24	2.30	2.73	3.08	2.03	3.17	2.90	2.67	4.25
	$\rho_{ad}$ (mmol/cm <sup>3</sup> )	13.73	14.50	14.27	14.35	14.53	14.81	14.13	13.81	13.90	14.60	13.87	14.06
	$\Delta n$ (mmol/g)	0.0064	0.0054	0.0064	0.0071	0.0054	0.0054	0.0059	0.0066	0.0044	0.0072	0.0051	0.0040
SDR- $\rho_{ad}$ model	$n_0$ (mmol/g)	0.199	0.245	0.223	0.280	0.144	0.247	0.233	0.149	0.275	0.433	0.402	0.320
	$D$	0.074	0.083	0.086	0.076	0.077	0.081	0.088	0.075	0.089	0.082	0.083	0.097
	$\rho_{ad}$ (mmol/cm <sup>3</sup> )	13.69	14.62	14.36	14.37	14.54	14.96	14.24	13.76	14.01	14.79	13.95	14.33
	$\Delta n$ (mmol/g)	0.0068	0.0058	0.0065	0.0078	0.0057	0.0059	0.0051	0.0070	0.0042	0.0061	0.0041	0.0030
Langmuir- $V_{ad}$ model	$n_0$ (mmol/g)	0.344	0.390	0.374	0.446	0.272	0.386	0.351	0.322	0.411	0.617	0.567	0.439
	$p_L$ (MPa)	3.41	3.40	3.65	3.15	4.03	3.27	3.20	4.74	3.18	2.87	2.73	3.00
	$V_{ad}$ (cm <sup>3</sup> /g)	0.022	0.023	0.023	0.027	0.016	0.023	0.022	0.020	0.026	0.037	0.036	0.028
	$\Delta n$ (mmol/g)	0.0019	0.0044	0.0044	0.0033	0.0016	0.0040	0.0055	0.0021	0.0069	0.0104	0.0085	0.0115
SDR- $V_{ad}$ model	$n_0$ (mmol/g)	0.207	0.257	0.235	0.293	0.151	0.259	0.245	0.155	0.290	0.456	0.422	0.340
	$D$	0.073	0.082	0.084	0.075	0.076	0.080	0.087	0.074	0.088	0.082	0.082	0.096
	$V_{ad}$ (cm <sup>3</sup> /g)	0.015	0.018	0.016	0.020	0.010	0.017	0.017	0.011	0.021	0.031	0.030	0.024
	$\rho_{ado}$ (mmol/cm <sup>3</sup> )	13.65	14.54	14.29	14.31	14.48	14.86	14.15	13.73	13.93	14.68	13.88	14.22
$\Delta n$ (mmol/g)	0.0073	0.0063	0.0071	0.0085	0.0061	0.0065	0.0056	0.0073	0.0050	0.0069	0.0051	0.0033	
	ARD (%)	23.78	10.55	14.31	13.51	17.94	9.78	13.73	24.20	10.73	7.36	8.79	6.35

$n_0$ : maximum absolute adsorption capacity;  $P_L$ : Langmuir pressure;  $\rho_{ad}$ : density of adsorbed gas phase;  $\Delta n$ : fitting error; ARD: average relative deviations;  $V_{ad}$ : volume of adsorbed gas phase;  $D$ : constant in SDR equations;  $\rho_{ado}$ : maximum density of adsorbed phase.

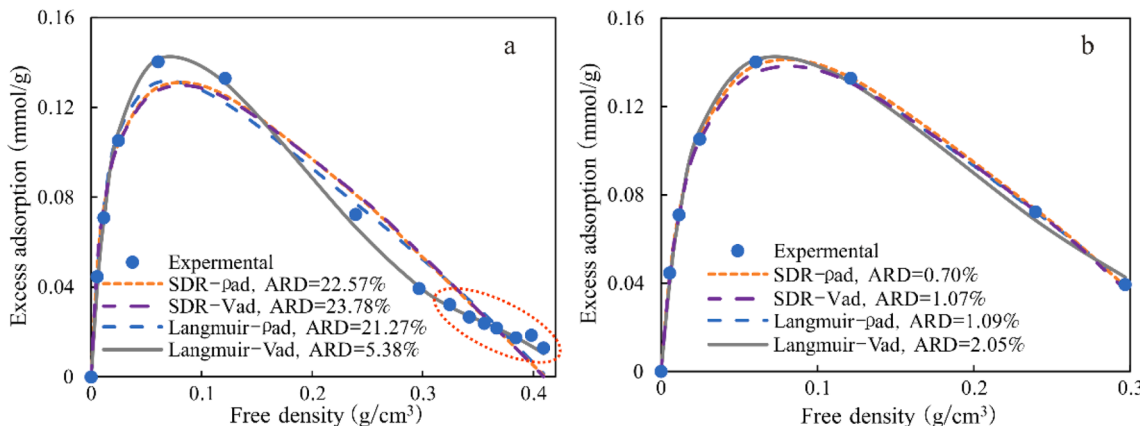


**Fig. 4.** Ethane excess adsorption versus free density curve for sample YK4 (a), note the “upwarp” part marked with red circle; fitting effects of models for ethane isotherm without the “upwarp” part.

#### ethane excess adsorption.

The raw data for binary gas adsorption amounts was in units of mg/g and could not be transformed into units of mmol/g directly because the proportion of methane or ethane in the adsorbed phase was not experimentally measured. In this study, the EL model and IAST model, combined with pure methane and ethane adsorption parameters obtained from the Langmuir- $V_{ad}$  model, were adopted to calculate mole fractions of methane and ethane in the adsorbed phase. Then density of the binary adsorbed phase was calculated and adopted to obtain binary gas excess adsorption amounts through Eq. (2). After which, the deviations between calculated and experimental ones were calculated to check the accuracy of the whole method. It should be noticed that, the Langmuir- $V_{ad}$  model involves a constant  $V_{ad}$  instead of  $\rho_{ad}$ , then a transform of Eq. (17) should be used in calculation of binary adsorbed phase density as follow:

$$\frac{1}{\rho_{ad-bin}(P)} = \frac{x_{meth}(P) \cdot n_{meth}^o(P)}{V_{meth}^o} + \frac{x_{eth}(P) \cdot n_{eth}^o(P)}{V_{eth}^o} \quad (21)$$

Here,  $\rho_{ad-bin}(P)$  is the density of binary adsorbed phase at pressure  $P$ ;  $x_{meth}(P)$  and  $x_{eth}(P)$  are the mole fractions of methane and ethane in binary adsorbed phase at pressure  $P$ , respectively;  $n_{meth}^o(P)$  and  $n_{eth}^o(P)$  are absolute adsorption amounts of pure methane and ethane at pressure  $P$ , respectively;  $V_{meth}^o$  and  $V_{eth}^o$  are the adsorbed phase volumes of methane and ethane obtained in the pure gas adsorption system, respectively.

The IAST and EL model-fitted total excess adsorption were both in good agreement with experimental results (Fig. 5). The average  $\Delta n$  and ARD for the IAST model were 0.144 mg/g and 7.74% respectively. Both the parameters were slightly lower than which in the EL model (0.146 mg/g and 7.78%, Table 3). The ARD for the IAST model obtained in this

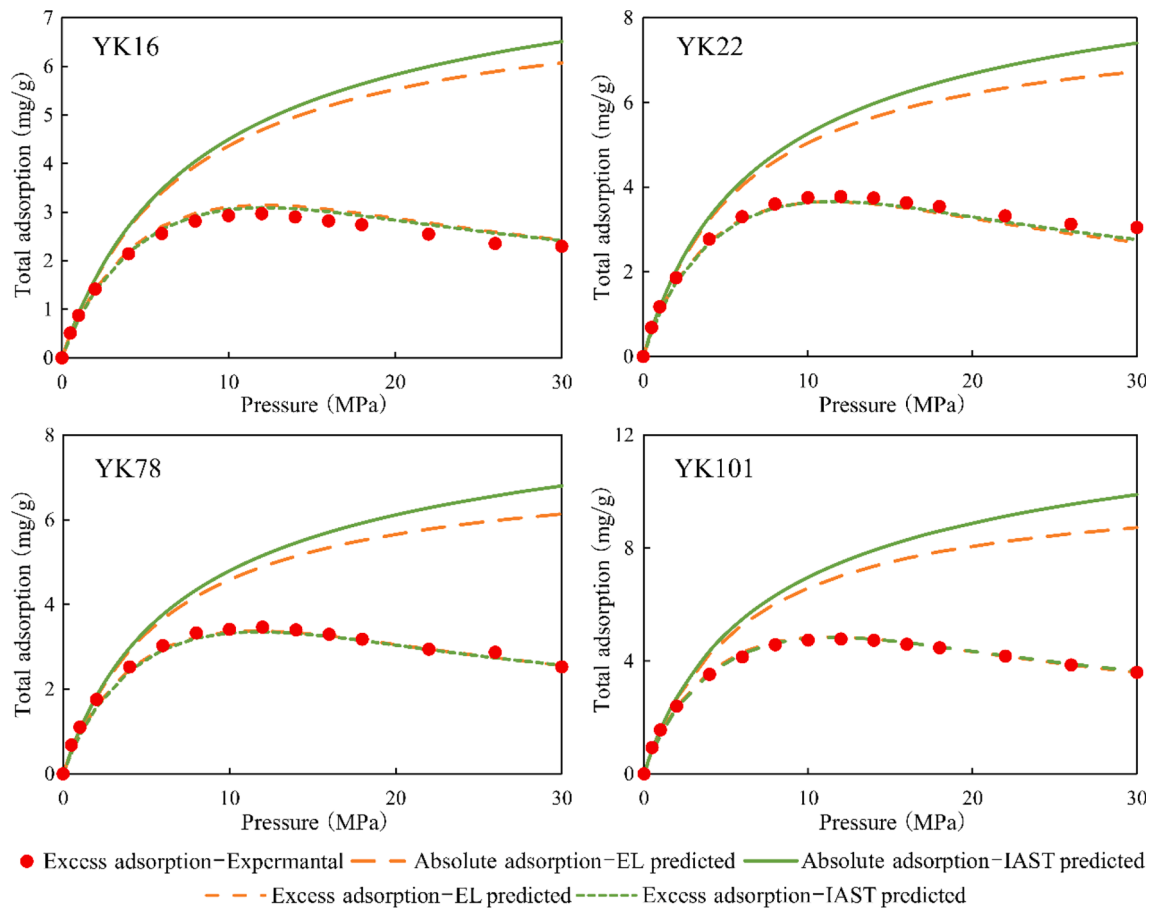


**Fig. 5.** Comparison of the EL and IAST models predictions for total binary gas adsorption isotherms and experimental results.

**Table 3**

## Fitted parameters of EL and IAST models for binary gas adsorption.

	YK4	YK16	YK18	YK22	YK29	YK42	YK49	YK55	YK78	YK93	YK101	YK107	
EL	$n_{total-30\text{ MPa}}$ (mmol/g)	0.234	0.261	0.235	0.296	0.154	0.232	0.226	0.194	0.268	0.373	0.368	0.276
	$n_{meth-30\text{ MPa}}$ (mmol/g)	0.119	0.126	0.113	0.153	0.080	0.110	0.114	0.104	0.137	0.192	0.166	0.130
	$n_{eth-30\text{ MPa}}$ (mmol/g)	0.115	0.135	0.122	0.142	0.074	0.121	0.112	0.090	0.132	0.181	0.202	0.147
	$\Delta n$ (mg/g)	0.280	0.144	0.366	0.130	0.140	0.142	0.096	0.137	0.074	0.100	0.069	0.077
	ARD (%)	14.11	6.57	19.13	5.44	10.38	8.19	5.31	8.50	4.54	4.32	3.02	3.87
	$S_{eth/meth}$	3.84	4.28	4.33	3.71	3.71	4.41	3.94	3.45	3.85	3.77	4.87	4.52
IAST	$n_{total-30\text{ MPa}}$ (mmol/g)	0.238	0.266	0.242	0.305	0.164	0.246	0.234	0.199	0.277	0.402	0.386	0.291
	$n_{meth-30\text{ MPa}}$ (mmol/g)	0.101	0.105	0.089	0.124	0.059	0.078	0.089	0.087	0.108	0.133	0.120	0.094
	$n_{eth-30\text{ MPa}}$ (mmol/g)	0.136	0.161	0.153	0.181	0.105	0.168	0.146	0.112	0.169	0.269	0.266	0.197
	$\Delta n$ (mg/g)	0.250	0.117	0.329	0.123	0.136	0.165	0.099	0.100	0.093	0.172	0.067	0.073
	ARD (%)	12.85	5.84	17.56	5.45	10.29	9.46	5.71	6.75	5.41	6.33	3.26	3.98
	$S_{eth/meth-10\text{ MPa}}$	4.52	5.07	5.40	4.64	5.07	6.10	5.06	4.15	4.88	5.52	6.53	6.10
	$S_{eth/meth-20\text{ MPa}}$	5.00	5.64	6.22	5.30	6.16	7.44	5.89	4.69	5.63	6.88	7.78	7.32
	$S_{eth/meth-30\text{ MPa}}$	5.38	6.10	6.91	5.85	7.14	8.63	6.58	5.14	6.25	8.07	8.85	8.37

$n_{total}$ -30 MPa: total adsorption of binary gas at 30 MPa;  $n_{meth}$ -30 MPa: methane adsorbed amount in binary gas adsorption at 30 MPa;  $n_{eth}$ -30 MPa: ethane adsorbed amount in binary gas adsorption at 30 MPa;  $\Delta n$ : fitting error; ARD: average relative deviations;  $S_{eth/meth}$ -10 MPa: adsorption selectivity of ethane over methane at 10 MPa;  $S_{eth/meth}$ -20 MPa: adsorption selectivity of ethane over methane at 20 MPa;  $S_{eth/meth}$ -30 MPa: adsorption selectivity of ethane over methane at 30 MPa.

study were close to that for total binary mixture (methane/carbon dioxide) adsorption on coal reported by Clarkson et al. [58].

$S_{eth/meth}$  fitted by the EL model was constant for a given studied sample under the measurement pressure and temperature in this study (Table 3). When involving the EL model (Eq. (11)), the equation of  $S_{eth/meth}$  (Eq. (18)) can be transformed into Eq. (22).

$$S_{eth/meth} = \frac{n_{0-eth} \cdot b_{eth}}{n_{0-meth} \cdot b_{meth}} \quad (22)$$

As shown in the above equation, the EL model-fitted  $S_{eth/meth}$  is independent of both pressure and mole fractions of free adsorbates. However, both the experimental and molecular simulation data revealed the variable adsorption selectivity with pressure or mole fractions of free adsorbates in binary mixture adsorption systems [26,29,30,51,59]. Besides, reasonable prediction of the IAST model for binary mixture adsorption in coal have been verified by Clarkson [58]. Sandoval et al [60] evaluated EL (so-called Multicomponent Langmuir in the literature), IAST and MPTA model predictions for binary gas adsorption on

shale. Results showed that for methane and ethane binary adsorption, the predictions of adsorbed amount were equally good in all methods. For adsorption selectivity prediction, the IAST gives good results while the EL prediction showed deviation. Therefore, predictions of the IAST model (Fig. A4) should be more reliable than which of the EL model.

### 3.2.2. Fitting results of binary gas adsorption

For the same sample, total absolute adsorbed amounts fitted by the IAST and EL model were close, while partial adsorbed amounts of methane or ethane obtained by different models showed significant deviations (Table 3). The mean of total absolute adsorbed amounts at 30 MPa ( $n_{total}$ -30 MPa) obtained by the IAST was 0.271 mmol/g and slightly higher than that obtained by the EL model (0.260 mmol/g). For the IAST, predicted partial adsorbed amounts of methane were significantly lower than those of ethane (Fig. A4), the averages of which were 0.099 mmol/g and 0.172 mmol/g at 30 MPa, respectively. However, approximately equal partial adsorbed amounts of methane and ethane were obtained by the EL model, the average of which at 30 MPa were 0.129 mmol/g and 0.131 mmol/g respectively. As discussed above, prediction of the IAST model should be more reliable and, therefore, were adopted

in the following calculation and discussion.

## 4. Discussion

### 4.1. Effect of shale components and nanopore characteristics on pure gas adsorption

Organic matter was the primary contributor to the pure gas adsorption capacities of the studied samples. Significant positive correlations between TOC and methane, ethane adsorption capacities were observed (Fig. 6a). The fitting slope for TOC versus ethane adsorption capacities was higher than which for TOC versus methane adsorption capacities, indicating a higher affinity of ethane than methane. Positive correlations between residual bitumen and pure gas adsorption capacities have also been observed (Fig. 6b). Residual bitumen existed in shale pores could dissolve gas then contribute to the gas adsorption capacity of shale [61]. According to our previous study, the proportion of dissolved methane on bitumen to adsorbed methane in the Yanchang shale could be higher than 36.23% [61].

As shown in the fitted lines of TOC versus pure gas adsorption

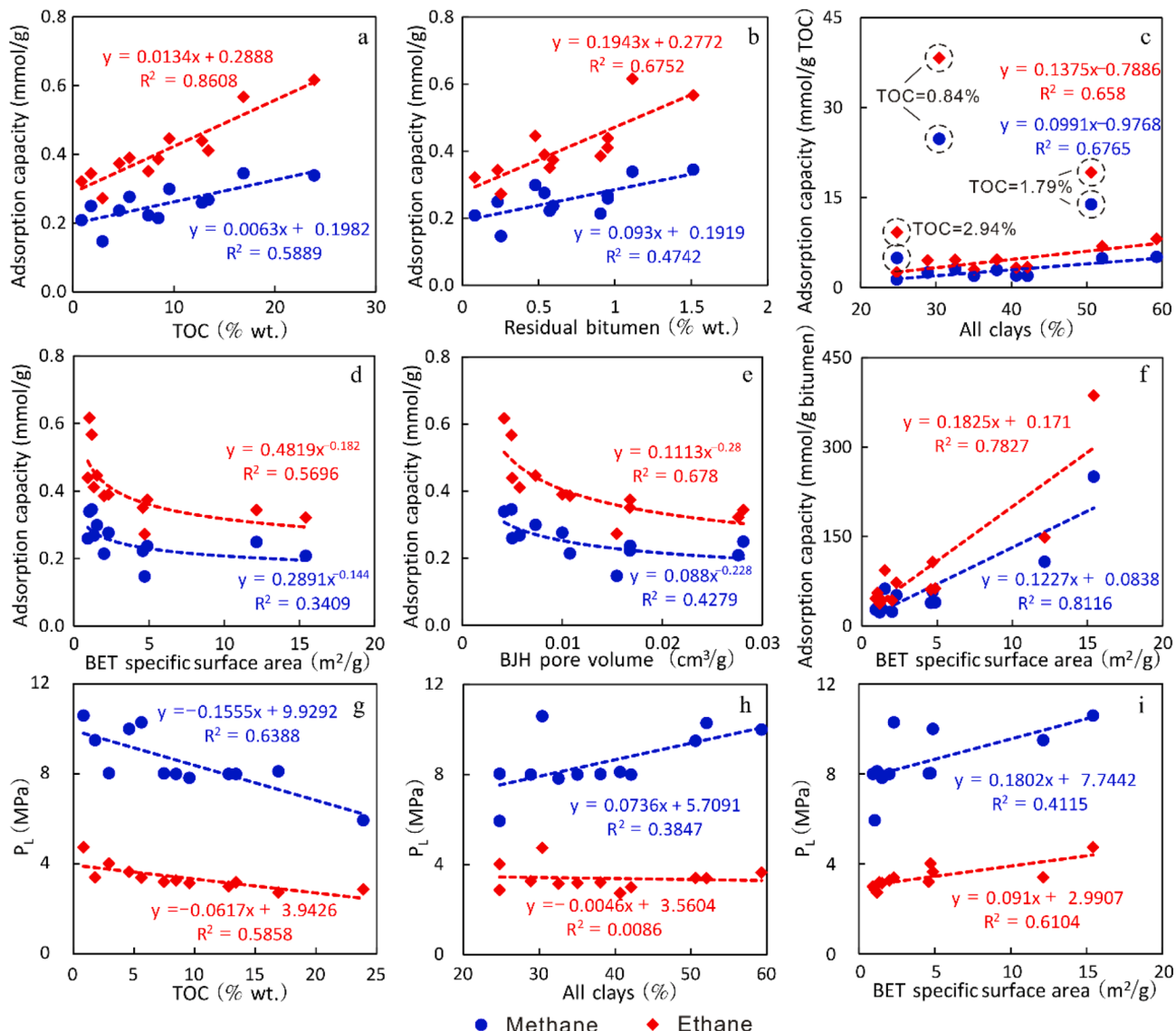


**Fig. 6.** Correlations between pure gas adsorption capacities and TOC (a), residual bitumen (b), BET specific surface area (d), BJH pore volume (e). Correlations between pure gas adsorption capacities normalized to TOC and all clays (c). Correlations between pure gas adsorption capacities normalized to residual bitumen content and BET specific surface area (f). Correlations between Langmuir pressure ( $P_L$ ) and TOC (g), all clays (h), BET specific surface area (i).

capacities (Fig. 6a), methane and ethane adsorption capacities did not approach 0 when TOC equals 0. This occurrence implied that shale components besides organic matter also contributed to pure gas adsorption capacity. When normalized to TOC, pure gas adsorption capacities of the studied samples (except the ones with low TOC values) showed weak positive correlations with clay mineral content (Fig. 6c) but showed no clear correlation with other mineral contents. This phenomenon indicated that clay was a minor contributor to pure gas adsorption capacity and was consistent with the observation of developed clay-related nanopores in the studied samples via FE-SEM images (Fig. A1). Besides, positive correlations between specific surface area and clay content in the Yanchang shale were also found in our previous study [38].

Inconsistent with traditional understanding, pure gas adsorption capacities revealed negative correlations with specific surface area and nanopore volume (Fig. 6d–e). It has been proved that residual bitumen occupied and blocked nanopores in the Yanchang shale resulting in negative correlations between nanoporosity and residual bitumen content [32,62–64]. Meanwhile, residual bitumen could dissolve gas thereby contribute significantly to gas adsorption capacity of shale [61]. Therefore, negative correlations between pure gas adsorption capacities

and specific surface area, nanopore volume were formed. When normalized to residual bitumen content, gas adsorption capacities revealed a significant positive correlation with specific surface area (Fig. 6f), which was consistent with the above interpretation.

Although a positive correlation between gas adsorption and residual bitumen content combined with a negative correlation between gas adsorption and nanopore surface area were observed in the studied shale, the conclusion of gas dissolution in bitumen higher than gas adsorption on pore surface remained elusive. For the sample YK93, which has a high bitumen content of 1.12%, a quantitative comparison of methane adsorption on the original and bitumen-free shale was conducted in our previous study [61]. The maximum absolute adsorption capacity decrease with percent of 26.29–36.23% after bitumen removal (Fig. A5). Those percentage seems to be contrary to the above correlations. However, given that shale specific surface area increases after extraction, the proportion of methane dissolution in methane adsorption could be higher than the decrease of adsorption after bitumen removal. Therefore, further studies are still needed to quantified methane dissolution in bitumen in organic-rich shale.

The Langmuir constant, which equals to the reciprocal of Langmuir pressure, is related to the affinity of an adsorbate for a surface. The

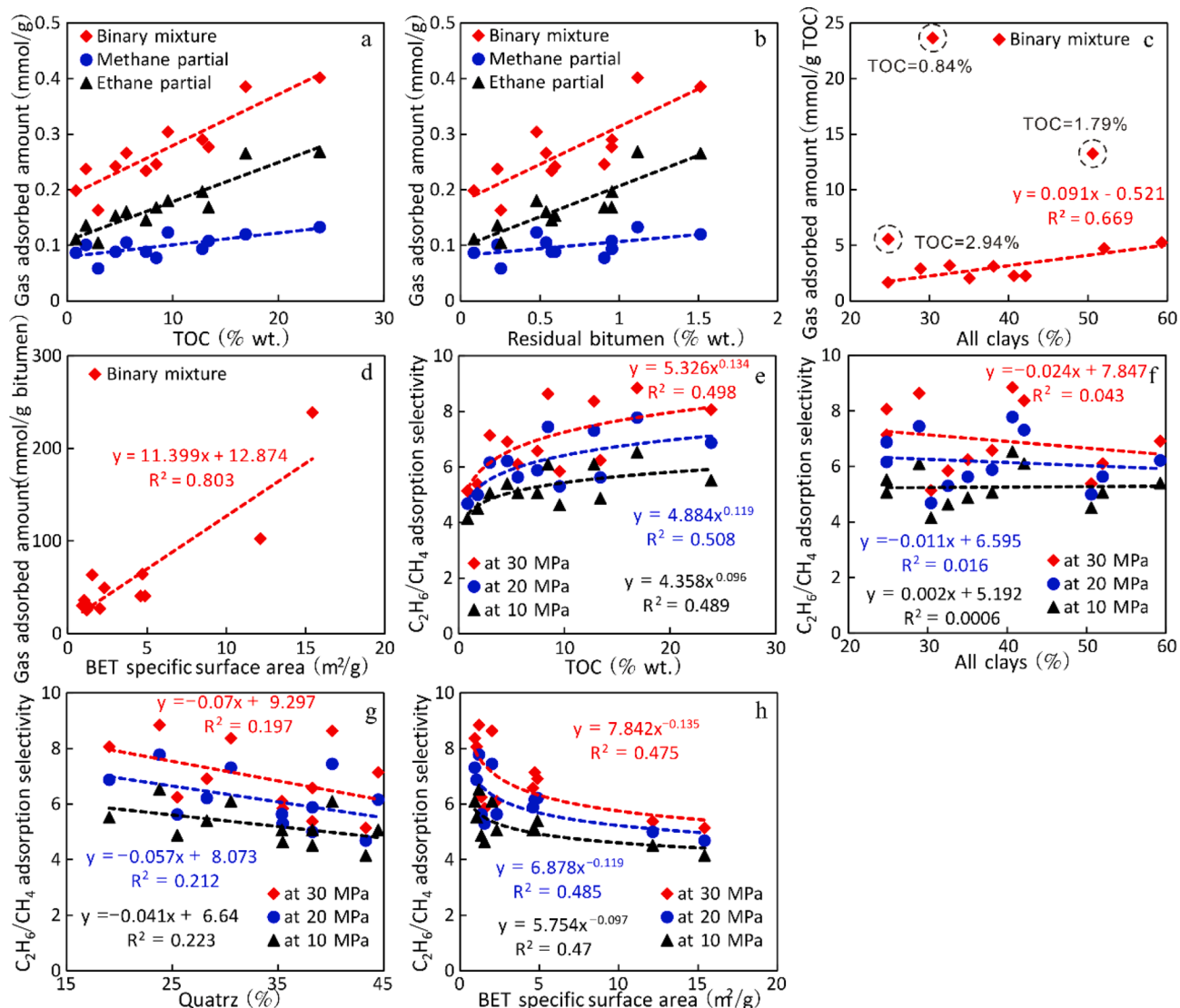


**Fig. 7.** Correlations between gas adsorbed amount at 30 MPa and TOC (a), residual bitumen (b). Correlations between gas adsorbed amount normalized to TOC at 30 MPa and all clays (c). Correlations between gas adsorbed amount normalized to residual bitumen content and BET specific surface area (d). Correlations between selectivity of ethane over methane and TOC (e), all clays (f), quartz (g), BET specific surface area (h).

higher Langmuir constant (i.e., the lower Langmuir pressure) indicates the stronger affinity [5]. The lower Langmuir pressure for ethane than for methane observed in this study was consistent with the qualitative classification of higher adsorption strength for ethane than for methane [25]. Significant negative correlations between TOC and Langmuir pressures for both methane and ethane were observed (Fig. 6g). Meanwhile, Langmuir pressure revealed weak positive correlations with clay mineral content (Fig. 6h). Those occurrences indicated stronger affinities of methane and ethane for organic matter than for clay mineral in shale. The variation of Langmuir pressure of methane was larger than that of ethane, indicating a larger difference in affinity of methane for different shale components. Positive correlations between Langmuir pressure and specific surface area were observed (Fig. 6i), which could be attributed to the significant negative correlation between specific surface area and TOC.

#### 4.2. Effect of shale components and nanopore characteristics on binary gas adsorption

Similar to pure gas adsorption, binary gas adsorption was also mainly controlled by organic matter content. Significant positive correlations between TOC, residual bitumen and binary gas adsorbed amount at 30 MPa were observed. With increasing TOC and residual bitumen, the increasing rate of ethane partial adsorption was higher than that of methane partial adsorption, which indicated a higher affinity of ethane than methane toward organic matter in the competitive adsorption (Fig. 7a, b).

Binary gas adsorbed amount at 30 MPa revealed weak positive relationships with clay content when normalized to TOC (Fig. 7c). This occurrence implied the minor contribution of clay-related pores to binary gas adsorption. Binary gas adsorbed amount at 30 MPa showed a clear positive correlation with specific surface area when normalized to residual bitumen content (Fig. 7d), reflecting the complex relationship between residual bitumen, nanopores and gas adsorption as discussed above.

Adsorption selectivity of ethane over methane ranged from 3.49 to 8.85 (Fig. A4). This value was close to those of a kerogen model obtained via molecular simulation (1.82–9.49) [26], but higher than those of a montmorillonite nanopore model obtained via molecular simulation (0.8–1.8) [29]. As discussed above, organic matter is the main contributor to gas adsorption of the studied samples. Then it is inferred that the adsorption selectivity of ethane over methane of organic matter could be higher than that of clay mineral.

For the studied samples, adsorption selectivity of ethane over methane increased with the increasing TOC (Fig. 7e) but showed weak decreasing trends with clay and quartz contents (Fig. 7f, g). These phenomena implied a higher adsorption selectivity for organic matter than for inorganic minerals, which was consistent with the previous inference. A negative correlation between adsorption selectivity and specific surface area was observed (Fig. 7h), the mechanism behind which could be the significant negative correlation between specific surface area and residual bitumen as reported in the previous study [32] and the positive correlation between organic matter content and adsorption selectivity (Fig. 7e).

Adsorption selectivity of ethane over methane obtained in this study showed increasing trend with pressure (Fig. A3). However, molecular simulation studies [26,29] revealed negative correlations between adsorption selectivity of ethane over methane and pressure. Moreover, a first increasing and later decreasing trend of the adsorption selectivity with pressure has also been reported in experimental study [30]. Gas adsorption selectivity in a porous material is usually caused by one or several of the following mechanisms: molecular sieving effect, thermodynamic equilibrium effect, kinetic effect and quantum sieving effect [25]. Among those mechanisms, molecular sieving effect, kinetic effect and quantum sieving effect are all related to pore size and adsorbates' kinetic diameter. Meanwhile, high pressure in the adsorption

measurement could cause shale matrix shrinkage and then affect pore size. Then the different relationship between adsorption selectivity and pressure could be attributed to the variety of nanopore characteristics for the studied samples.

#### 4.3. Estimations of geological gas-in-place (GIP)

In the previous sections, we showed the adsorption behaviors of pure or binary mixture of methane and ethane on shale and their relationships with shale components and nanopore characteristics. To gain better insights into shale gas exploration, gas-in-place (GIP) of the Yanchang shale was estimated in this section based on the adsorption data and pressure and temperature conditions for the corresponding formation.

GIP is a crucial parameter in the exploration for shale gas. It is an estimation of the maximum amount of gas that can be stored in the respective rock and equals to the sum of adsorbed and free gas capacities (Fig. 8a) [20]. The pressure coefficient of 7.4 MPa/km [65] and geothermal gradient of 28 °C/km [66] of the Ordos Basin were used to build hydrostatic pressure and temperature progression with depth. Adsorbed gas capacities of binary mixture were estimated via the IAST model. Free gas capacities were estimated based on the pore volume obtained via helium porosity measurement (Table A3) and gas density obtained via the Peng-Robinson equation of state (PR-EOS) [67]. Subsequently, GIP was calculated by summing the adsorbed and free gas capacities up. In this study, gas adsorption for the studied shale samples were measured at a single temperature of 60 °C, corresponding to a depth of 1667 m which is within the burial depth of the Yanchang Formation (600 m–2000 m) [24]. Therefore, the subsequent discussion focused on the GIP of the formation at 1667 m depth. The GIP was expressed in cm<sup>3</sup>/g for the convenience of geological application.

The average GIP for binary mixture of 80% methane and 20% ethane at depth of 1667 m ranged from 4.57 cm<sup>3</sup>/g to 8.08 cm<sup>3</sup>/g, which was about 30% larger than the value for pure methane (Fig. 8b). Therefore, the traditional approach of GIP estimation basing on pure methane adsorption data may significantly underestimate shale gas potential. A two-stage trend in the relationship between binary gas GIP and organic matter content was observed (Fig. 8c, d). GIP decreased with increasing TOC and residual bitumen content first, reached the lowest position at TOC of about 5%, then increased. This occurrence could be attributed to the high content of residual bitumen in the studied samples and its dual effects on GIP estimation. On one hand, residual bitumen could occupy and block the nanopores thereby reduce the free gas capacity [64,68,69]. On the other hand, residual bitumen could dissolve gas and significantly contribute to the adsorbed gas capacity [61,63]. According to the observations of this study, the effect of residual bitumen on free gas capacity was more significant than that on adsorbed gas capacity in the samples with TOC lower than 5%. While in the samples with TOC larger than 5%, the situation was opposite. Proportion of adsorbed gas in GIP ranged from 50.74% to 90.3% and revealed an increasing trend with the increasing TOC (Fig. 8e).

#### 5. Conclusions

The current study presented systematic experimental data for adsorption of pure methane, ethane and their binary mixture on organic-rich lacustrine shale. The Langmuir model, SDR model, EL model and IAST model were used to describe the adsorption data. The main conclusions are as follows:

(1) With increasing pressure, the measured excess adsorption for pure methane, ethane and their binary mixture all presented first increase then decrease curves. A steep decline followed by an inflection was observed in ethane excess adsorption isotherms. All models fitted methane excess adsorption isotherm equally well, while for ethane adsorption the Langmuir model with a constant of  $V_{ad}$  matched the isotherms significantly better. For binary adsorption, The IAST and EL

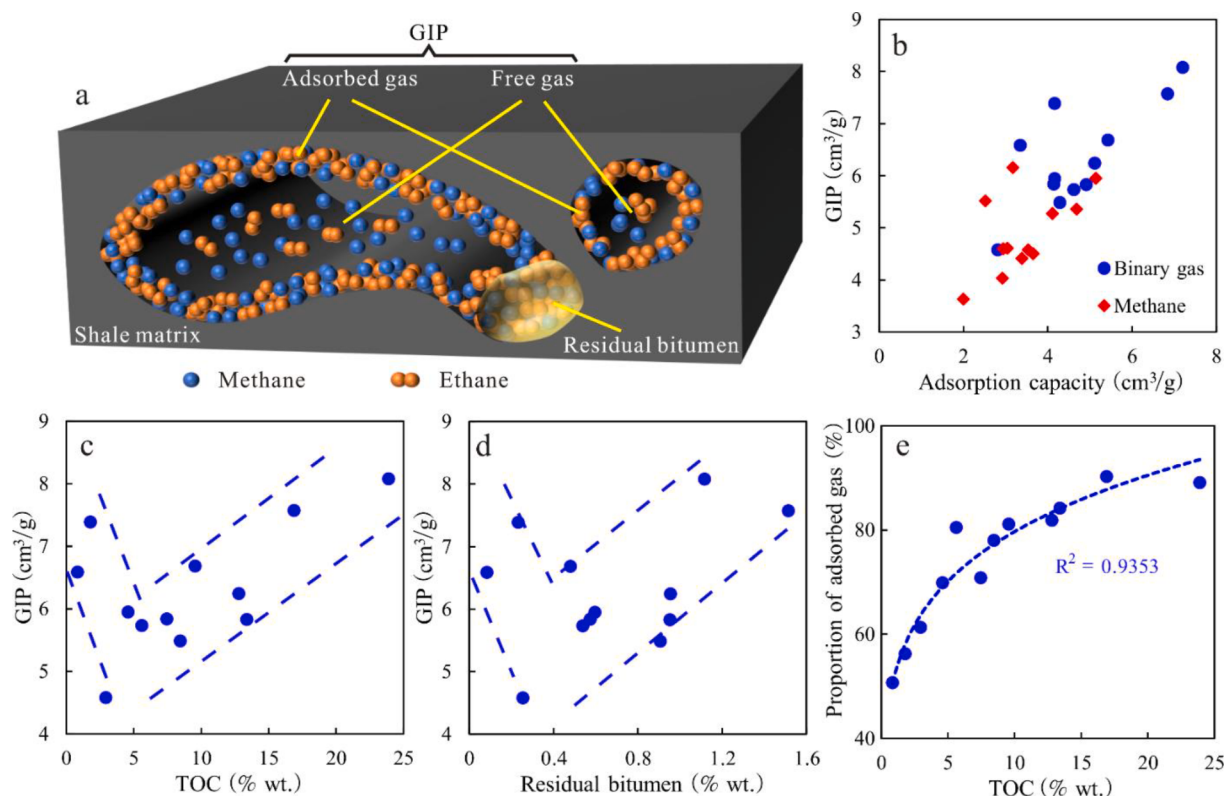


**Fig. 8.** Schematic representation of GIP for binary gas (a). Comparison between GIP for binary gas and for methane at depth of 1667 m (b). Correlations between GIP for binary gas and TOC (c), residual bitumen (d) at depth of 1667 m. Correlation between proportion of adsorbed binary gas and TOC (e).

models matched experimental results equally well.

(2) For pure gas adsorption, the maximum adsorption for ethane was about 1.6 times larger than that for methane, while the Langmuir pressure for ethane was lower. For binary gas adsorption, the adsorption selectivity of ethane over methane ranged from 3.49 to 8.85, which strongly depended on total organic carbon (TOC), and weakly negatively correlated with clay mineral content. For the adsorption of pure and binary gas, organic matter was the primary contributor, followed by clay minerals.

(3) The estimated GIP of binary gas for the studied samples ranged from  $4.57 \text{ cm}^3/\text{g}$  to  $8.08 \text{ cm}^3/\text{g}$ , which was about 30% larger than that of pure methane. This phenomenon indicated a considerable underestimation of shale gas potential for the conventional approach basing on pure methane adsorption. A two-stage trend in relationship between binary gas GIP and organic matter content was observed. With increasing TOC, GIP decreased first, reaching the lowest value at TOC of about 5%, then increased. This occurrence could be attributed to the high content of residual bitumen and its opposite effects on shale porosity and gas adsorption.

#### Declaration of Competing Interest

The authors declare the following financial interests/personal relationships which may be considered as potential competing interests: Jing Li reports financial support was provided by National Natural Science Foundation of China.

#### Acknowledgments

This work was supported by the National Natural Science Foundation of China (Grant No. 42172178), the “Light of West China” Program of the Chinese Academy of Sciences and the Project of Stable Support for Youth Team in Basic Research Field, Chinese Academy of Sciences

(Grant No. YSBR-017). The authors would like to appreciate Dr. Jianjun Liang, who has greatly improved the quality of this paper.

#### Appendix A. Supplementary data

Supplementary data to this article can be found online at <https://doi.org/10.1016/j.cej.2022.136617>.

#### References

- [1] J.B. Curtis, Fractured shale-gas systems, AAPG Bull. 86 (11) (2002) 1921–1938, <https://doi.org/10.1306/61EEDDBE-173E-11D7-8645000102C1865D>.
- [2] S.L. Montgomery, D.M. Jarvie, K.A. Bowker, R.M. Pollastro, Mississippian Barnett Shale, Fort Worth basin, north-central Texas: gas-shale play with multi-trillion cubic foot potential, AAPG Bull. 89 (2) (2005) 155–175, <https://doi.org/10.1306/09170404042>.
- [3] Energy Information Administration, Natural Gas Annual (updated September 30, 2021). <<https://www.eia.gov/naturalgas/annual/>>, 2021 (accessed February 8, 2022).
- [4] C. Zou, Q. Zhao, L. Cong, H. Wang, Z. Shi, J. Wu, S. Pan, Development progress, potential and prospect of shale gas in China, Nat. Gas Ind. 41 (1) (2021) 1–14, <https://doi.org/10.3787/j.isnn.1000-0976.2021.01.001>.
- [5] T. Zhang, G.S. Ellis, S.C. Ruppel, K. Milliken, R. Yang, Effect of organic-matter type and thermal maturity on methane adsorption in shale-gas systems, Org. Geochem. 47 (2012) 120–131, <https://doi.org/10.1016/j.orggeochem.2012.03.012>.
- [6] T.F. Rexer, E.J. Mathia, A.C. Aplin, K.M. Thomas, High-pressure methane adsorption and characterization of pores in *posidonia* shales and isolated kerogens, Energ. Fuel 28 (5) (2014) 2886–2901, <https://doi.org/10.1021/ef402466m>.
- [7] T. Zhao, X. Li, H. Zhao, M. Li, Molecular simulation of adsorption and thermodynamic properties on type II kerogen: Influence of maturity and moisture content, Fuel 190 (2017) 198–207, <https://doi.org/10.1016/j.fuel.2016.11.027>.
- [8] Y. Pang, Y. Tian, M.Y. Soliman, Y. Shen, Experimental measurement and analytical estimation of methane absorption in shale kerogen, Fuel 240 (2019) 192–205, <https://doi.org/10.1016/j.fuel.2018.11.144>.
- [9] L. Ji, T. Zhang, K.L. Milliken, J. Qu, X. Zhang, Experimental investigation of main controls to methane adsorption in clay-rich rocks, Appl. Geochem. 27 (12) (2012) 2533–2545, <https://doi.org/10.1016/j.apgeochem.2012.08.027>.
- [10] E. Fan, S. Tang, C. Zhang, Q. Guo, C. Sun, Methane sorption capacity of organics and clays in high-over matured shale-gas systems, Energy Explor. Exploit. 32 (6) (2014) 927–942, <https://doi.org/10.1260/0144-5987.32.6.927>.

- [11] Y. Gu, W. Ding, S. Yin, M. Yin, Z. Xiao, Adsorption characteristics of clay minerals in shale, *Pet. Sci. Technol.* 36 (2) (2017) 108–114, <https://doi.org/10.1080/10916466.2017.1405031>.
- [12] M. Gasparik, A. Ghanizadeh, P. Bertier, Y. Gensterblum, S. Bouw, B.M. Krooss, High-pressure methane sorption isotherms of black shales from The Netherlands, *Energ Fuel* 26 (8) (2012) 4995–5004, <https://doi.org/10.1021/ef300405g>.
- [13] K. Zeng, T. Lu, P. Jiang, B. Zhou, R. Xu, Methane adsorption capacity measurement in shale matrix nanopores at high pressure by low-field NMR and molecular simulation, *Chem. Eng. J.* 430 (2022), 133151, <https://doi.org/10.1016/j.cej.2021.133151>.
- [14] L. Chen, L. Zuo, Z. Jiang, S. Jiang, K. Liu, J. Tan, L. Zhang, Mechanisms of shale gas adsorption: evidence from thermodynamics and kinetics study of methane adsorption on shale, *Chem. Eng. J.* 361 (2019) 559–570, <https://doi.org/10.1016/j.cej.2018.11.185>.
- [15] H. Guo, W. Jia, P. Peng, Y. Lei, X. Luo, M. Cheng, X. Wang, L. Zhang, C. Jiang, The composition and its impact on the methane sorption of lacustrine shales from the Upper Triassic Yanchang Formation, Ordos Basin, China, *Mar. Pet. Geol.* 57 (2014) 509–520.
- [16] M. Gasparik, P. Bertier, Y. Gensterblum, A. Ghanizadeh, B.M. Krooss, R. Little, Geological controls on the methane storage capacity in organic-rich shales, *Int. J. Coal Geol.* 123 (2014) 34–51, <https://doi.org/10.1016/j.coal.2013.06.010>.
- [17] R. Hu, W. Wang, J. Tan, L. Chen, J. Dick, G. He, Mechanisms of shale gas adsorption: Insights from a comparative study on a thermodynamic investigation of microfossil-rich shale and non-microfossil shale, *Chem. Eng. J.* 411 (2021), 128463, <https://doi.org/10.1016/j.cej.2021.128463>.
- [18] W. Jiang, G. Cao, C. Luo, M. Lin, L. Ji, J. Zhou, A composition-based model for methane adsorption of overmature shales in Wufeng and Longmaxi formation, Sichuan Basin, *Chem. Eng. J.* 429 (2022), 130766, <https://doi.org/10.1016/j.cej.2021.130766>.
- [19] R.J. Ambrose, R.C. Hartman, M. Diaz-Campos, I.Y. Akkutlu, C.H. Sondergeld, Shale gas-in-place calculations part I: new pore-scale considerations, *SPE J.* 17 (1) (2012) 219–229, <https://doi.org/10.2118/131772-PA>.
- [20] H. Tian, T. Li, T. Zhang, X. Xiao, Characterization of methane adsorption on overmature Lower Silurian–Upper Ordovician shales in Sichuan Basin, southwest China: experimental results and geological implications, *Int. J. Coal Geol.* 156 (2016) 36–49, <https://doi.org/10.1016/j.coal.2016.01.013>.
- [21] J. Li, S. Zhou, G. Gaus, Y. Li, Y. Ma, K. Chen, Y. Zhang, Characterization of methane adsorption on shale and isolated kerogen from the Sichuan Basin under pressure up to 60 MPa: experimental results and geological implications, *Int. J. Coal Geol.* 189 (2018) 83–93, <https://doi.org/10.1016/j.coal.2018.02.020>.
- [22] K.A. Bullin, P.E. Krouskop, Compositional variety complicates processing plans for US shale gas, *Oil Gas J.* 107 (10) (2009) 50–55.
- [23] M. Zhang, Q. Tang, C. Cao, Z. Lv, T. Zhang, D. Zhang, Z. Li, L. Du, Molecular and carbon isotopic variation in 3.5 years shale gas production from Longmaxi Formation in Sichuan Basin, China, *Mar. Pet. Geol.* 89 (2018) 27–37, <https://doi.org/10.1016/j.marpetgeo.2017.01.023>.
- [24] X.Z. Wang, Y.H. Lei, X.F. Wang, Genesis types and sources of Mesozoic Lacustrine shale gas in the Southern Ordos Basin, NW China, *Energy Explor. Exploit.* 33 (3) (2015) 317–337, <https://doi.org/10.1260/0144-5987.33.3.317>.
- [25] J.R. Li, R.J. Kuppler, H.C. Zhou, Selective gas adsorption and separation in metal-organic frameworks, *Chem. Soc. Rev.* 38 (5) (2009) 1477–1504, <https://doi.org/10.1039/b802426j>.
- [26] J. Collell, G. Galliero, F. Gouth, F. Montel, M. Pujol, P. Ungerer, M. Yiannourakou, Molecular simulation and modelisation of methane/ethane mixtures adsorption onto a microporous molecular model of kerogen under typical reservoir conditions, *Micropor. Mesopor. Mat.* 197 (2014) 194–203, <https://doi.org/10.1016/j.micromeso.2014.06.016>.
- [27] Y. Wang, T.T. Tsotis, K. Jessen, Competitive sorption of methane/ethane mixtures on shale: measurements and modeling, *Ind. Eng. Chem. Res.* 54 (48) (2015) 12187–12195, <https://doi.org/10.1021/acs.iecr.5b02850>.
- [28] D. Dasani, Y. Wang, T.T. Tsotis, K. Jessen, Laboratory-scale investigation of sorption kinetics of methane/ethane mixtures in shale, *Ind. Eng. Chem. Res.* 56 (36) (2017) 9953–9963, <https://doi.org/10.1021/acs.iecr.7b02431>.
- [29] S. Wang, Q. Feng, F. Javadpour, Q. Hu, K. Wu, Competitive adsorption of methane and ethane in montmorillonite nanopores of shale at supercritical conditions: a grand canonical Monte Carlo simulation study, *Chem. Eng. J.* 355 (2019) 76–90, <https://doi.org/10.1016/j.cej.2018.08.067>.
- [30] L. Huang, Z. Ning, H. Lin, W. Zhou, L. Wang, J. Zou, H. Xu, High-pressure sorption of methane, ethane, and their mixtures on shales from Sichuan basin, China, *Energ Fuel* 35 (5) (2021) 3989–3999, <https://doi.org/10.1021/acs.energyfuels.0c04205>.
- [31] X.Z. Wang, Jinchuan; Cao, Jinzhou; Zhang, Lixia; Tang, Xuan; Lin, Lamei; Jiang, Chengfu; Yang, Yiting; Wang, Long; Wu, Ying, A preliminary discussion on evaluation of continental shale gas resources: a case study of Chang 7 of Mesozoic Yanchang Formation in Zhihuo-Xiasawan area of Yanchang, *Earth Sci. Front.* 19 (2012) 192–197. [https://doi.org/10.1016/S1872-2040\(11\)60566-5](https://doi.org/10.1016/S1872-2040(11)60566-5).
- [32] J. Li, S. Zhou, Y. Li, Y. Ma, Y. Yang, C. Li, Effect of organic matter on pore structure of mature lacustrine organic-rich shale: a case study of the Triassic Yanchang shale, Ordos Basin, China, *Fuel* 185 (2016) 421–431, <https://doi.org/10.1016/j.fuel.2016.07.100>.
- [33] S. Brunauer, P.H. Emmett, E. Teller, Adsorption of gases in multimolecular layers, *J. Am. Chem. Soc.* 60 (2) (1938) 309–319, <https://doi.org/10.1021/ja01269a023>.
- [34] E.P. Barrett, L.G. Joyner, P.P. Halenda, The determination of pore volume and area distributions in porous substances. 1. Computations from nitrogen isotherms, *J. Am. Chem. Soc.* 73 (1) (1951) 373–380, <https://doi.org/10.1021/ja01145a126>.
- [35] M.M. Dubinin, Physical Adsorption of Gases and Vapors in Micropores, in: D.A. Cadenhead, J.F. Danielli, M.D. Rosenberg (Eds.), *Progress in Surface and Membrane Science*, Elsevier1975, pp. 1–70. <https://doi.org/10.1016/B978-0-12-571809-7.50006-1>.
- [36] C. Lastoskie, K.E. Gubbins, N. Quirke, Pore size heterogeneity and the carbon slit pore: a density functional theory model, *Langmuir* 9 (10) (2002) 2693–2702, <https://doi.org/10.1021/la00034a032>.
- [37] K.S.W. Sing, Reporting physisorption data for gas, solid systems with special reference to the determination of surface area and porosity (Recommendations 1984), *Pure Appl. Chem.* 57 (1985) 603–619.
- [38] J. Li, P. Li, S. Zhou, B. Meng, Z. Sun, X. Zhang, Opposite contributions of types I and II organic matter to nanoporosity in lacustrine shale, *Nat. Resour. Res.* 30 (6) (2021) 4843–4859, <https://doi.org/10.1007/s11053-021-09946-x>.
- [39] F. Dreisbach, H.W. Lösch, P. Harting, Highest pressure adsorption equilibria data: measurement with magnetic suspension balance and analysis with a new adsorbent/adsorbate-volume, *Adsorption* 8 (2) (2002) 95–109, <https://doi.org/10.1023/A:1020431616093>.
- [40] J.U. Keller, R. Staudt, *Gas Adsorption Equilibria: Experimental Methods and Adsorptive Isotherms*, Springer Science & Business Media Inc., Boston, USA, 2005.
- [41] M. Gasparik, T.F.T. Rexer, A.C. Aplin, P. Billemont, G. De Weireld, Y. Gensterblum, M. Henry, B.M. Krooss, S. Liu, X. Ma, R. Sakurovs, Z. Song, G. Staib, K.M. Thomas, S. Wang, T. Zhang, First international inter-laboratory comparison of high-pressure CH<sub>4</sub>, CO<sub>2</sub> and C2H<sub>6</sub> sorption isotherms on carbonaceous shales, *Int. J. Coal Geol.* 132 (1) (2014) 131–146, <https://doi.org/10.1016/j.coal.2014.07.010>.
- [42] X. Tang, N. Ripepi, N.P. Stadie, L. Yu, M.R. Hall, A dual-site Langmuir equation for accurate estimation of high pressure deep shale gas resources, *Fuel* 185 (2016) 10–17, <https://doi.org/10.1016/j.fuel.2016.07.088>.
- [43] S. Sircar, Gibbsian surface excess for gas adsorption - Revisited, *Ind. Eng. Chem. Res.* 38 (10) (1999) 3670–3682, <https://doi.org/10.1021/ie9900871>.
- [44] I. Langmuir, The adsorption of gases on plane surfaces of glass, mica and platinum, *J. Am. Chem. Soc.* 40 (1918) 1361–1403, <https://doi.org/10.1021/ja02242a004>.
- [45] K. Kaneko, K. Murata, An analytical method of micropore filling of a supercritical gas, *Adsorption* 3 (3) (1997) 197–208, <https://doi.org/10.1007/bf01650131>.
- [46] R. Sakurovs, S. Day, S. Weir, G. Duffy, Application of a modified Dubinin–Radushkevich equation to adsorption of gases by coals under supercritical conditions, *Energ Fuel* 21 (2) (2007) 992–997, <https://doi.org/10.1021/ef0600614>.
- [47] C.R. Clarkson, B. Haghshenas, Modeling of Supercritical Fluid Adsorption on Organic-Rich Shales and Coal, Paper presented at the SPE Unconventional Resources Conference-USA, The Woodlands, Texas, USA, April 2013. <https://doi.org/10.2118/164532-MS>.
- [48] M. Meng, R. Zhong, Z. Wei, Prediction of methane adsorption in shale: Classical models and machine learning based models, *Fuel* 278 (2020), 118358, <https://doi.org/10.1016/j.fuel.2020.118358>.
- [49] M. Sudibandriyo, Z. Pan, J.E. Fitzgerald, R.L. Robinson, K.A.M. Gasem, Adsorption of methane, nitrogen, carbon dioxide, and their binary mixtures on dry activated carbon at 318.2 K and pressures up to 13.6 MPa, *Langmuir* 19 (13) (2003) 5323–5331.
- [50] R.T. Yang, Chapter, 2 - Adsorbents and Adsorption Isotherms, in: R.T. Yang (Ed.), *Gas Separation by Adsorption Processes*, Butterworth-Heinemann, Boston, 1987, pp. 9–48, <https://doi.org/10.1016/b978-0-409-90004-0.50005-2>.
- [51] C.R. Clarkson, Application of a new multicomponent gas adsorption model to coal gas adsorption systems, *SPE J.* 8 (3) (2003) 236–251, <https://doi.org/10.2118/78146-PA>.
- [52] K.S. Walton, D.S. Sholl, Predicting multicomponent adsorption: 50 years of the ideal adsorbed solution theory, *AIChE J.* 61 (9) (2015) 2757–2762, <https://doi.org/10.1002/aiic.14878>.
- [53] A.L. Myers, J.M. Prausnitz, Thermodynamics of mixed-gas adsorption, *AIChE J.* 11 (1) (1965) 121–127.
- [54] N.F. Cessford, N.A. Seaton, T. Düren, Evaluation of ideal adsorbed solution theory as a tool for the design of metal-organic framework materials, *Ind. Eng. Chem. Res.* 51 (13) (2012) 4911–4921, <https://doi.org/10.1021/ie202219w>.
- [55] Y. Kurniawan, S.K. Bhatia, V. Rudolph, Simulation of binary mixture adsorption of methane and CO<sub>2</sub> at supercritical conditions in carbons, *AIChE J.* 52 (3) (2006) 957–967, <https://doi.org/10.1002/aiic.10687>.
- [56] P. Weniger, W. Kalkreuth, A. Busch, B.M. Krooss, High-pressure methane and carbon dioxide sorption on coal and shale samples from the Paraná Basin, Brazil, *Int. J. Coal Geol.* 84 (3) (2010) 190–205, <https://doi.org/10.1016/j.jcoalgeol.2010.08.003>.
- [57] R.J. Ambrose, R.C. Hartman, I.Y. Akkutlu, Multi-Component Sorbed-Phase Considerations for Shale Gas-in-place Calculations, Paper presented at the SPE Production and Operations Symposium, Oklahoma City, Oklahoma, USA, March 2011. <https://doi.org/10.2118/141416-ms>.
- [58] C.R. Clarkson, R.M. Bustein, Binary gas adsorption/desorption isotherms: effect of moisture and coal composition upon carbon dioxide selectivity over methane, *Int. J. Coal Geol.* 42 (4) (2000) 241–271, [https://doi.org/10.1016/S0166-5162\(99\)00032-4](https://doi.org/10.1016/S0166-5162(99)00032-4).
- [59] R. Qi, Z. Ning, Q. Wang, Y. Zeng, L. Huang, S. Zhang, H. Du, Sorption of methane, carbon dioxide, and their mixtures on shales from Sichuan Basin, China, *Energ. Fuel* 32 (3) (2018) 2926–2940, <https://doi.org/10.1021/acs.energyfuels.7b03429>.
- [60] D.R. Sandoval, W. Yan, M.L. Michelsen, E.H. Stenby, Modeling of shale gas adsorption and its influence on phase equilibrium, *Ind. Eng. Chem. Res.* 57 (17) (2018) 5736–5747, <https://doi.org/10.1021/acs.iecr.7b04144>.
- [61] J. Li, S. Zhou, D. Fu, K. Chen, C. Zhang, Z. Sun, P. Li, Quantitative gas-in-place comparison of original and bitumen-free lacustrine shale, *Acta Geol. Sin. - Engl.* (2021), <https://doi.org/10.1111/1755-6724.14680>.
- [62] G. Liu, Z. Huang, Z. Jiang, J. Chen, F. Chen, J. Xing, Gas adsorption capacity calculation limitation due to methane adsorption in low thermal maturity shale: a

- case study from the Yanchang Formation, Ordos Basin, *J. Nat. Gas. Sci. Eng.* 30 (2016) 106–118, <https://doi.org/10.1016/j.jngse.2016.01.026>.
- [63] F. Xiong, Z. Jiang, J. Chen, X. Wang, Z. Huang, G. Liu, F. Chen, Y. Li, L. Chen, L. Zhang, The role of the residual bitumen in the gas storage capacity of mature lacustrine shale: a case study of the Triassic Yanchang shale, Ordos Basin, China, *Mar. Pet. Geol.* 69 (2016) 205–215, <https://doi.org/10.1016/j.marpetgeo.2015.10.022>.
- [64] H. Guo, R. He, W. Jia, P. Peng, Y. Lei, X. Luo, X. Wang, L. Zhang, C. Jiang, Pore characteristics of lacustrine shale within the oil window in the Upper Triassic Yanchang Formation, southeastern Ordos Basin, China, *Mar. Pet. Geol.* 91 (2018) 279–296.
- [65] S. Li, Z. Shi, X. Liu, S. Yang, X. Deng, G. Liu, J. Li, Quantitative analysis of the Mesozoic abnormal low pressure in Ordos Basin, *Petrol. Explor. Dev.* 40 (5) (2013) 566–571, [https://doi.org/10.1016/S1876-3804\(13\)60074-9](https://doi.org/10.1016/S1876-3804(13)60074-9).
- [66] Z. Ren, Q. Yu, J. Cui, K. Qi, Z. Chen, Z. Cao, P. Yang, Thermal history and its controls on oil and gas of the Ordos Basin, *Earth Sci. Front.* 24 (3) (2017) 137–148, <https://doi.org/10.13745/j.esf.2017.03.012>.
- [67] P.M. Mathias, T.W. Copeman, Extension of the Peng-Robinson equation of state to complex mixtures: evaluation of the various forms of the local composition concept, *Fluid Phase Equilib.* 13 (1983) 91–108, [https://doi.org/10.1016/0378-3812\(83\)80084-3](https://doi.org/10.1016/0378-3812(83)80084-3).
- [68] L. Wei, M. Mastalerz, A. Schimmelmann, Y. Chen, Influence of Soxhlet-extractable bitumen and oil on porosity in thermally maturing organic-rich shales, *Int. J. Coal Geol.* 132 (2014) 38–50, <https://doi.org/10.1016/j.coal.2014.08.003>.
- [69] Y. Cao, H. Han, H.-W. Liu, J.-C. Jia, W. Zhang, P.-W. Liu, Z.-G. Ding, S.-J. Chen, J.-G. Lu, Y. Gao, Influence of solvents on pore structure and methane adsorption capacity of lacustrine shales: an example from a Chang 7 shale sample in the Ordos Basin, China, *J. Petrol. Sci. Eng.* 178 (2019) 419–428, <https://doi.org/10.1016/j.petrol.2019.03.052>.